Consistency and bicharacteristic analysis of integral porosity shallow water models. Explaining model oversensitivity to mesh design

Vincent Guinot

Consistency and bicharacteristic analysis of integral porosity shallow water models. Explaining model oversensitivity to mesh design

Vincent Guinot

Université de Montpellier, UMR HSM, 163 rue Auguste Broussonnet, 34090 Montpellier, France

Inria Lemon, Bât 5 – CC05 017, 860 rue Saint-Priest, 34095 Montpellier Cedex 5, France

This is the preprint of a paper accepted for publication in *Advances in Water Resources.*
DOI: 10.1016/j.advwatres.2017.06.008.
URL: http://www.sciencedirect.com/science/article/pii/S0309170817301380

Abstract

The Integral Porosity and Dual Integral Porosity two-dimensional shallow water models have been proposed recently as efficient upscaled models for urban floods. Very little is known so far about their consistency and wave propagation properties. Simple numerical experiments show that both models are unusually sensitive to the computational grid. In the present paper, a two-dimensional consistency and characteristic analysis is carried out for these two models. The following results are obtained: (i) the models are almost insensitive to grid design when the porosity is isotropic, (ii) anisotropic porosity fields induce an artificial polarization of the mass/momentum fluxes along preferential directions when triangular meshes are used and (iii) extra first-order derivatives appear in the governing equations when regular, quadrangular cells are used. The hyperbolic system is thus mesh-dependent, and with it the wave propagation properties of the model solutions. Criteria are derived to make the solution less mesh-dependent, but it is not certain that these criteria can be satisfied at all computational points when real-world situations are dealt with.

1 Introduction

Two-dimensional porosity-based shallow water models for urban flood modelling have gained popularity over the past decade. With computational times reduced by two to three orders of magnitude compared to refined shallow water models, they appear as a promising option for upscaling the shallow water equations in the urban environment. Originally, these models incorporated only one type of porosity and were formulated in differential form [5, 11, 13]. Most developments so far have focused on this isotropic, Single Porosity (SP) version [1, 2, 6, 21]. The methods proposed to address the anisotropy of the urban medium use several types of porosity instead of a single one. Such models include the Multiple Porosity (MP) model [9] and the Integral Porosity (IP) model [18]. The salient features of the IP approach are that (i) a differential formulation for such models is deemed meaningless in that the urban medium is not continuous on the scale at

which the porosity model is used, (ii) two types of porosity are distinguished: a storage porosity, that represents the volume fraction available for mass and momentum storage, and a connectivity porosity, that accounts for the connectivity of the urban medium, thus acting on the computation of fluxes. This formulation is well-suited to finite volume, shock-capturing numerical techniques. The latest developments available from the literature include depth-variable IP models [16] and the Dual Integral Porosity (DIP) model [12]. Laboratory and numerical experiments have shown the superiority of the IP approach over the SP [14]. The DIP model yields improved wave propagation properties over the IP model [12].

The IP/DIP approach allows the anisotropy of the urban medium to be characterized very easily via the connectivity porosity. In finite volume discretizations (that are the only family of discretizations proposed so far for such models), the connectivity porosity is defined for each cell interface from the intersection with building contours [18, 19]. This makes its numerical value strongly dependent on the mesh design, as opposed to the SP [11] and MP [9] approaches, that use a domain-based statistical definition for the porosity. In [18], various meshing strategies are proposed, all leading to different values for the connectivity porosities. While these strategies are compared in terms of computational effort, little is known on their influence on the accuracy of the porosity model apart from the study reported in [19]

Although the differential form of the porosity equations is deemed meaningless in the integral approach, [9, 12] show that the differential expression of the governing equations gives useful and accurate information of the wave propagation properties of the porosity model. However, only the one-dimensional version of the IP/DIP equations has been analysed [10, 12]. No full 2D analysis has been provided so far, although the first steps of such an analysis were made in [15] for a particular case of the IP model. The purpose of the present paper is to provide such an analysis for both the IP and DIP model and to draw consequences in terms of IP/DIP solution behaviour and accuracy.

The need for a two-dimensional analysis stems from the recently observed unusual sensitivity of the IP and DIP model to the design of the computational mesh (see Subsection 2.2). Such oversensitivity seems never to have been observed before (see e.g. [19] for a successful field scale application of the IP model using different mesh resolutions and different porosity parametrization methods). It is not observed with the SP and MP models [9, 11, 20], that use identical storage and connectivity porosities. This leads to wonder whether the oversensitivity of the IP/DIP model to grid design arises from the dual definition (domain- and boundary-based) of porosity or from specific features of the mesh design.

This paper is organised as follows. In Section 2, the oversensitivity of the IP/DIP model to mesh design is illustrated by a simple computational example. Such oversensitivity is explained by a two-dimensional consistency analysis. In Section 3, a two-dimensional characteristic analysis is carried out for the IP and DIP models. It is illustrated with numerical examples in Section 4. Section 5 provides guidelines for the design of IP/DIP meshes and conclusions.

2 Consistency analysis of the IP/DIP models

2.1 Overview of the models

The governing equations for the Integral Porosity (IP) [18] and Dual Integral Porosity (DIP) [12] models are obtained by applying mass and momentum balances to a control volume Ω with

boundary Γ

$$\partial_t \int_\Omega \phi_\Omega h \mathrm{d}\Omega + \int_\Gamma \phi_\Gamma \mathbf{q}_\Gamma.\mathbf{n}\, \mathrm{d}\Gamma = 0 \tag{1a}$$

$$\partial_t \int_\Omega \phi_\Omega \mathbf{q} \mathrm{d}\Omega + \int_\Gamma \phi_\Gamma \left[(\mathbf{q}_\Gamma.\mathbf{n})\, \mathbf{q}_\Gamma + \frac{g}{2} h_\Gamma^2 \mathbf{n} \right] \mathrm{d}\Gamma = \int_\Omega \mathbf{s}_\Omega \mathrm{d}\Omega + \int_\Omega \mathbf{s}_\Gamma \mathrm{d}\Gamma \tag{1b}$$

where g is the gravitational acceleration, h and h_Γ are respectively the water depth over Ω and Γ, $\mathbf{n}$ is the outwards normal unit vector to the boundary, $\mathbf{q}$ and $\mathbf{q}_\Gamma$ are the unit discharge vectors over Ω and Γ, ϕ_Ω and ϕ_Γ are respectively the storage and connectivity porosity, $\mathbf{s}_\Omega$ is the momentum source term arising from the bottom slope and friction onto the bottom, $\mathbf{s}_\Gamma$ is the momentum source term arising from energy dissipation due to building drag and the reaction to the pressure force exerted by the building walls onto the water. The detailed expression for $\mathbf{s}_\Omega$ and $\mathbf{s}_\Gamma$ can be found in [18]. It is not important at this stage because the present study focuses on the wave propagation properties of the model, in situations where the source terms are zero. In what follows, the following assumptions are thus retained: horizontal, frictionless bottom and negligible building drag forces.

In the IP model [18], the following closure is assumed between the domain and boundary variables:

$$h_\Gamma = h, \;\; \mathbf{q}_\Gamma = \mathbf{q} \tag{2}$$

The closure introduced in the DIP model is shown in [12] to provide a better upscaling of the shallow water equations:

$$h_\Gamma = h, \;\; \mathbf{q}_\Gamma = \frac{\phi_\Omega}{\phi_\Gamma} \mathbf{q} \tag{3}$$

This closure model is shown in [12] to have a strong influence on the wave propagation properties of the solutions. However, the analysis in [12] is restricted to one-dimensional flow configurations.

2.2 Oversensitivity to grid design: a simple example

Consider an idealized urban layout made of square house blocks of identical size, regularly spaced along the $x-$ and $y-$directions (Figure 1). Let a, L_x and L_y be respectively the block width and the $x-$ and $y-$spatial periods of the urban layout. Using the IP and DIP models require that a storage and connectivity porosity be defined for this layout. The storage porosity is defined as the fraction of space available to water storage, that is $\phi_\Omega = 1 - \frac{a^2}{L_x L_y}$.

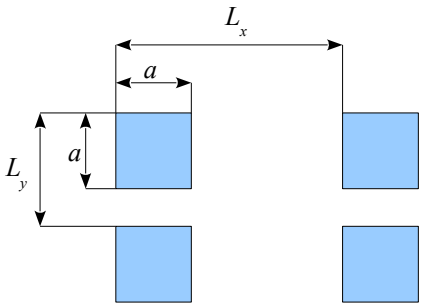

Figure 1: Periodic, idealized urban layout. Definition sketch. Only one period is shown in each direction of space.

According to [18], the definition of the connectivity porosity is not unique and depends on the

meshing strategy used to solve the IP equations numerically. Figure 2 shows three possible mesh designs. In the first (Figure 2a), rectangular cells are defined from the centroids of the building blocks. The connectivity porosity is $\phi_1 = 1 - \frac{a}{L_y}$ along the vertical edges and $\phi_2 = 1 - \frac{a}{L_x}$ along the horizontal edges. In the second mesh design (Figure 2b), the computational cells are parallelograms with corners located at the centroids of the blocks. The connectivity porosity is ϕ_1 along the vertical edges and ϕ_2 along the diagonal edges (assuming $L_x > L_y$). The third mesh design (Figure 2c) is the union of the previous two, which results in right-angled triangular cells whose corners are again the centroids of the house blocks. In this design, the connectivity porosity is ϕ_1 along the vertical edge and ϕ_2 along the horizontal edge. Along the hypotenuse, it is ϕ_2 if $L_x > L_y$ and ϕ_1 otherwise.

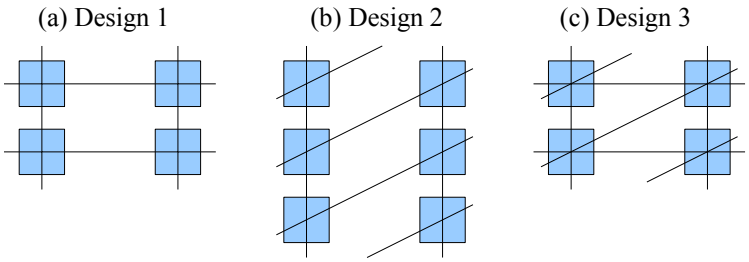

Figure 2: Three possible mesh design strategies for the periodic urban layout in Figure 1.

Mesh designs 1 to 3 are used to simulate the propagation of a wave into a semi-infinite building layout using the IP model. The initial and boundary conditions are illustrated in Figure 3. The bottom is flat, motion is assumed frictionless. The water is initially at rest, at a depth $h = h_0$ and a zero velocity at all points. The boundary condition is a zero mass flux across the Western boundary, except over a region of length L, where the constant depth $h = h_1 \neq h_0$ is prescribed from $t = 0$ onwards. A wave is generated and propagates into the domain. The semi-infinite domain is simulated by generating a large mesh and stopping the simulation before the wave reaches the mesh boundaries. The governing equations are solved using a finite volume procedure detailed in [18]. The fluxes are computed using a modified HLLC Riemann solver [12].

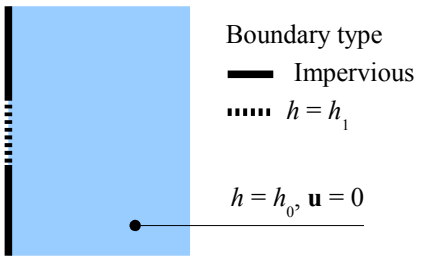

Figure 3: Propagation of a wave into a semi-infinite domain. Definition sketch for initial and boundary conditions.

The parameters of the test case are given in Table 1.

Symbol	Meaning	Numerical value
a	Size of the square house block	10m
g	Gravitational acceleration	9.81ms^{-2}
h_0	Initial water depth	1m
h_1	Prescribed water depth at the boundary	1.1m
L	Length of the prescribed water depth boundary	100m
L_x	$x-$period of the layout	30m
L_y	$y-$period of the layout	15m
ϕ_1	Connectivity porosity along the vertical edges	1/3
ϕ_2	Connectivity porosity along the horizontal and diagonal edges	2/3
ϕ_Ω	Storage porosity	7/9

Table 1: Test case parameters.

Figure 4 shows the water depth computed at $t = 200$s using the three mesh designs. While Design 1 leads to the expected symmetrical water depth field (Figure 4a), the symmetry is broken by Design 2 (Figure 4b). With Design 3, the propagation of the wave in the $x-$direction is almost stopped (save for a slight front smearing due to the numerical diffusion of the Riemann solver) and propagation occurs only along the $y-$direction. This simple experiment shows the extreme sensitivity of the IP model to grid design. This oversensitivity is shown in the next two subsections to arise from consistency issues.

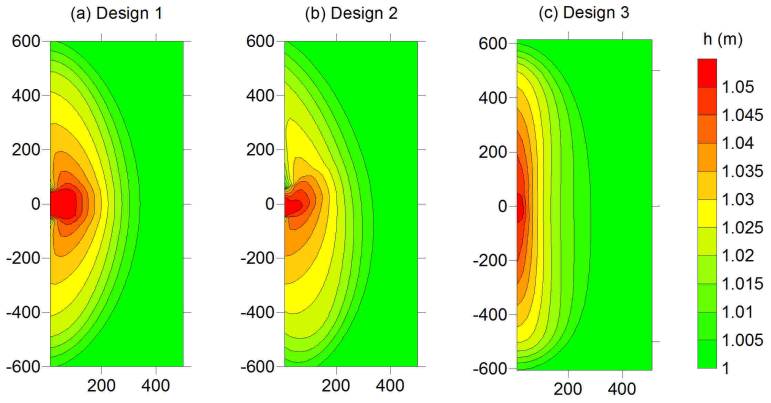

Figure 4: Propagation of a wave into a semi-infinite domain. Simulation results at $t = 200$s. $x-$ and $y-$coordinates in metres.

2.3 Consistency issue 1: flux polarization

Consider the continuity equation for the IP model, obtained by substituting the closure model (2) into the continuity equation (1a):

$$\partial_t \int_\Omega \phi_\Omega h \mathrm{d}\Omega + \int_\Gamma \phi_\Gamma \mathbf{q}.\mathbf{n}\mathrm{d}\Gamma = 0 \tag{4}$$

A salient feature of the IP model [18] is that the connectivity porosity is not isotropic (in contrast with the domain porosity) and therefore is a function of both $\mathbf{n}$ and the location on the boundary. When the equations are solved numerically, the domain Ω is a computational cell, usually triangular or quadrangular. The present subsection aims to investigate the behaviour of the integral formulation as the grid is refined, as in a consistency and numerical convergence analysis. In such an analysis, only the size of the cell changes. Its shape and the distribution of the porosity over

the cell edges remain identical.

In the limit of an infinitesimal domain Ω, the differential form of the equation is meaningful and the divergence of $\phi_\Gamma \mathbf{q}$ is defined as

$$\nabla \left(\phi_\Gamma \mathbf{q} \right) = \frac{1}{\Omega} \int_\Gamma \phi_\Gamma \mathbf{q}.\mathbf{n} \mathrm{d}\Gamma \tag{5}$$

where Ω is the area of the domain. A first-order Taylor series expansion yields the following first-order approximation for the divergence of $\phi_\Gamma \mathbf{q}$:

$$\begin{array}{rcl} \nabla.\left(\phi_\Gamma \mathbf{q} \right) & \approx & \frac{1}{\Omega} \int_\Gamma \phi_\Gamma \left(\mathbf{q}_\mathrm{G} + \nabla \mathbf{q}\, \mathbf{v} \right) .\mathbf{n} \mathrm{d}\Gamma \\ & = & \frac{1}{\Omega} \mathbf{q}_\mathrm{G}. \int_\Gamma \phi_\Gamma \mathbf{n} \mathrm{d}\Gamma + \frac{1}{\Omega} \int_\Gamma \phi_\Gamma \left(\nabla \mathbf{q}\, \mathbf{v} \right) .\mathbf{n} \mathrm{d}\Gamma \end{array} \tag{6}$$

where $\mathbf{q}_\mathrm{G}$ is the point value for $\mathbf{q}$ at the centre of mass G of Ω, $\mathbf{v}$ is the vector connecting G with the centre M of the infinitesimal $\mathrm{d}\Gamma$ (Figure 5) and $\nabla \mathbf{q}$ is the gradient of the vector field $\mathbf{q}$:

$$\nabla \mathbf{q} = \left[\begin{array}{cc} \partial_x q_x & \partial_y q_x \\ \partial_x q_y & \partial_y q_y \end{array} \right] \tag{7}$$

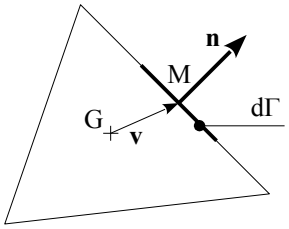

Figure 5: Consistency analysis. Definition sketch.

Assume now that the domain is scaled by a factor $\kappa < 1$ (in a numerical convergence analysis, $\kappa \to 0$). The distribution of ϕ_Γ does not change along Γ because it is a function of $\mathbf{n}$ alone. Then

$$\int_\Gamma \phi_\Gamma \mathbf{n} \mathrm{d}\Gamma \propto \kappa \tag{8a}$$

$$\mathbf{v} \propto \kappa \Rightarrow \int_\Gamma \phi_\Gamma \left(\nabla \mathbf{q}\, \mathbf{v} \right) .\mathbf{n} \mathrm{d}\Gamma \propto \kappa^2 \tag{8b}$$

$$\Omega \propto \kappa^2 \tag{8c}$$

The first equality stems from the fact that the size of the integration domain is proportional to κ. In the second integral, the vector $\mathbf{v}$, that is proportional to κ, is integrated along the boundary, the size of which is also proportional to κ. The size of Ω being proportional to κ^2, it follows that

$$\frac{1}{\Omega} \mathbf{q}_\mathrm{G}. \int_\Gamma \phi_\Gamma \mathbf{n} \mathrm{d}\Gamma \propto \frac{1}{\kappa} \tag{9}$$

Therefore the divergence of the mass flux tends to infinity as the size of the domain tends to zero. The existence of continuous solutions implies

$$\mathbf{q}_\mathrm{G}. \int_\Gamma \phi_\Gamma \mathbf{n} \mathrm{d}\Gamma = 0 \ \ \forall \mathbf{q} \tag{10}$$

This condition is satisfied in one of the following two situations:

(i) The integral $\int_\Gamma \phi_\Gamma \mathbf{n} \mathrm{d}\Gamma$ is zero. This is true when ϕ_Γ is uniform over Γ. This is for instance the case in the SP model [11], in the IP and DIP models when the urban layout is isotropic. Note that in the DIP model, the porosity in the flux of the continuity equation is isotropic because of the closure model for the unit discharge. However, the boundary porosity in the momentum equation is anisotropic, and problems similar to the IP model are encountered (see computational examples in Section 4). This case is also encountered in the mesh designs 1 and 2. In both designs, ϕ_Γ is not uniform along the cell boundaries, but it takes identical values on opposite edges, that also have the same length and orientation.

(ii) The integral $\int_\Gamma \phi_\Gamma \mathbf{n} \mathrm{d}\Gamma$ is non-zero. Then the gradient of ϕ_Γ over Ω tends to infinity as the size of Ω tends to zero. The existence of a continuous solution implies that $\mathbf{q}$ is orthogonal to $\int_\Gamma \phi_\Gamma \mathbf{n} \mathrm{d}\Gamma$. This entails an artificial polarization of the mass flux in the direction orthogonal to the integral. This configuration occurs with the third mesh design presented in the above computational example. In the example of section 2.1, the vector integral $\int_\Gamma \phi_\Gamma \mathbf{n} \mathrm{d}\Gamma$ is collinear with the $x-$axis. This enforces unit discharges vectors oriented in the $y-$direction. This explains the strongly polarized $h-$field and the scattering in the $x-$direction.

The above analysis has been carried out only for the mass flux in the IP model. It is also valid for the momentum flux in the IP and in the DIP models. Therefore, both models can be expected to exhibit an artificial polarization of the hydrodynamic fields as soon as the condition (10) is violated.

2.4 Consistency issue 2: mesh-dependent governing equations

The first and second mesh designs satisfy the constraint (10). The consistency of the integral equation is analysed for a computational cell with width and height are respectively $\mathrm{d}x$ and $\mathrm{d}y$. The Northern and Southern edges of the cell are parallel to the $x-$axis, while the Eastern and Western edges make an angle α with the $y-$axis (Figure 6). Mesh Design 2 can be retrieved from this design by applying a 90 degree clockwise rotation to Figure 6.

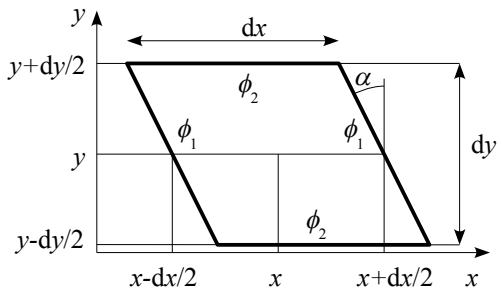

Figure 6: Quadrangular cell.

For a flux vector $\mathbf{f} = [f_x, f_y]^T$, a first-order Taylor series expansion yields the following limit as $(\mathrm{d}x, \mathrm{d}y) \to (0,0)$

$$\frac{1}{\Omega} \int_\Gamma \phi_\Gamma \mathbf{f}.\mathbf{n} \, \mathrm{d}\Gamma \underset{(\mathrm{d}x,\mathrm{d}y)\to(0,0)}{\longrightarrow} \partial_x \left(\phi_1 f_x + (\phi_1 - \phi_2) \tan\alpha f_y \right) + \partial_y \left(\phi_2 f_y \right) \tag{11}$$

In the general case the expression of the divergence of $\phi_\Gamma \mathbf{f}$ (and with it the governing equations) is explicitly dependent on the orientation of the Eastern and Western edges of the control volume. It is independent from α only if $(\phi_1 - \phi_2)\tan\alpha = \text{Const}$. If this is the case then there exists α_0, ϕ_1^0 such that

$$(\phi_1 - \phi_2)\tan\alpha = \left(\phi_1^0 - \phi_2\right)\tan\alpha_0 \tag{12}$$

and therefore

$$\phi_1 = \phi_2 + \left(\phi_1^0 - \phi_2\right)\frac{\tan\alpha_0}{\tan\alpha} \tag{13}$$

There are two particular cases where this is always true. The first is $\phi_1^0 = \phi_2$. The second is $\alpha_0 = 0$. Both cases lead to the isotropic case, $\phi_1 = \phi_2$. If $\phi_1 = \phi_2 = \phi$, then one has

$$\frac{1}{\Omega}\int_\Gamma \phi_\Gamma \mathbf{f}.\mathbf{n}\,\mathrm{d}\Gamma \underset{(\mathrm{d}x,\mathrm{d}y)\to(0,0)}{\longrightarrow} \partial_x\left(\phi f_x\right) + \partial_y\left(\phi f_y\right) \tag{14}$$

an expression that is independent of the cell edge orientation.

In the case of an anisotropic layout, one has

$$\alpha \in [\alpha_{\min}, \alpha_{\max}] \Leftrightarrow \phi_1 \in [0,1] \tag{15a}$$

$$\alpha_{\min} = \tan^{-1}\left[\left(1 - \frac{\phi_1^0}{\phi_2}\right)\tan\alpha_0\right] \tag{15b}$$

$$\alpha_{\max} = \tan^{-1}\left[\left(\frac{\phi_1^0 - \phi_2}{1 - \phi_2}\right)\tan\alpha_0\right] \tag{15c}$$

As an obvious consequence, the porosity should not be defined independently from the orientation of the edges of the computational cells. The original approach used in [12, 14, 18], whereby the boundary porosity is derived directly from building geometry, does in most cases not fulfil the condition (13).

3 Wave propagation properties: characteristic analysis

3.1 Characteristic analysis in two dimensions of space

The wave propagation properties are analysed for a mesh design that is free from any polarization issue. The configuration of Figure 6, that contains both Designs 1 and 2, is retained in what follows. There are two main methods to carry out a characteristic analysis [8]. Both derive from the non-conservation form of the equations

$$\partial_t \mathbf{u} + \mathbf{A}_x \partial_x \mathbf{u} + \mathbf{A}_y \partial_y \mathbf{u} = 0 \tag{16}$$

In a first approach, used in e.g. [4, 7] the characteristic (sometimes referred to as bicharacteristic) surfaces in the (x, y, t) space are defined as

$$t = \tau(x, y) \tag{17a}$$

$$|\mathbf{I} - \partial_x \tau \mathbf{A}_x - \partial_y \tau \mathbf{A}_y| = 0 \tag{17b}$$

In the second approach, called the secant plane approach, the system is analysed in one dimension of space [8]. The equations are rewritten in the coordinate system (x', y') obtained by rotating

the (x, y) coordinate system by an angle θ (Figure 7). The solution is assumed one-dimensional in x', thus obeying the following governing equation

$$\partial_t \mathbf{u} + \mathbf{A}_\theta \partial_{x'} \mathbf{u} = 0, \quad \mathbf{A}_\theta = \cos\theta \mathbf{A}_x + \sin\theta \mathbf{A}_y \tag{18}$$

The eigenvalues λ of $\mathbf{A}_\theta$ are the wave propagation speeds in the direction x', called the secant direction. The characteristic planes $\mathrm{d}x' = \lambda \mathrm{d}t$ are straight lines in the secant planes. The characteristic surfaces are obtained as the envelopes of the characteristic planes by spanning the range $\theta \in [0, 2\pi]$. Assuming that an eigenvalue λ has been found in the direction x' of the secant plane, the general equation for the envelope is obtained from a simple variation analysis as

$$\mathrm{d}_t \begin{bmatrix} x \\ y \end{bmatrix} = \begin{bmatrix} \cos\theta & -\sin\theta \\ \sin\theta & \cos\theta \end{bmatrix} \begin{bmatrix} \lambda \\ \partial_\theta \lambda \end{bmatrix} \tag{19}$$

The secant plane approach has the interest that the directions of minimum and maximum extension of the characteristic surfaces can be identified very easily. This approach is retained in what follows.

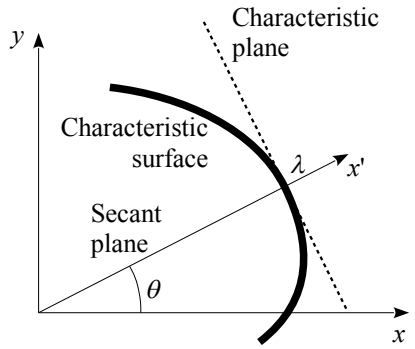

Figure 7: Secant plane approach. Intersections of the secant plane, characteristic plane and characteristic surface with the horizontal plane $t = \text{Const}$. The characteristic surface is the envelope of the characteristic planes obtained by varying θ.

3.2 Analysis of the IP model

Tangent planes. In the absence of source term due to friction, porosity gradient and bottom slope, the source term in the continuity and momentum equations is zero. From equation (11), the differential conservation form for the governing equations for the IP model over a quadrangular mesh as defined in Figure 5 is (see A.1 for a detailed derivation)

$$\partial_t \mathbf{u} + \nabla . \mathbf{F} = 0 \tag{20a}$$

$$\mathbf{F} = \begin{bmatrix} \epsilon_1 hu + \epsilon_3 hv & \epsilon_2 hv \\ \epsilon_1 \left(hu^2 + \frac{g}{2}h^2\right) + \epsilon_3 huv & \epsilon_2 huv \\ \epsilon_1 huv + \epsilon_3 \left(hv^2 + \frac{g}{2}h^2\right) & \epsilon_2 \left(hv^2 + \frac{g}{2}h^2\right) \end{bmatrix} \tag{20b}$$

$$\epsilon_1 = \frac{\phi_1}{\phi}, \quad \epsilon_2 = \frac{\phi_2}{\phi}, \quad \epsilon_3 = \frac{(\phi_1 - \phi_2)\tan\alpha}{\phi} \tag{20c}$$

The expression for the matrix $\mathbf{A}_\theta$ follows directly (see Section A.1.3 in the Appendix for the details):

$$\mathbf{A}_\theta = \cos\theta \mathbf{A}_x + \sin\theta \mathbf{A}_y = \begin{bmatrix} 0 & \epsilon_1 \cos\theta & \epsilon_5 \\ \left(c^2 - u^2\right)\epsilon_4 - \epsilon_5 uv & 2\epsilon_4 + \epsilon_5 v & \epsilon_5 u \\ \left(c^2 - v^2\right)\epsilon_5 - \epsilon_4 uv & \epsilon_4 v & \epsilon_4 u + 2\epsilon_5 v \end{bmatrix} \tag{21a}$$

$$\epsilon_4 = \epsilon_1 \cos\theta, \;\; \epsilon_5 = \epsilon_2 \sin\theta + \epsilon_3 \cos\theta \tag{21b}$$

The eigenvalues of $\mathbf{A}_\theta$ are

$$\lambda_p = \epsilon_4 u + \epsilon_5 v + (p-2)\left(\epsilon_4^2 + \epsilon_5^2\right)^{\frac{1}{2}} c, \;\; p = 1, 2, 3 \tag{22}$$

There are three characteristic planes defined by

$$\mathrm{d}_t x_p = \lambda_p \cos\theta \tag{23a}$$

$$\mathrm{d}_t y_p = \lambda_p \sin\theta \tag{23b}$$

Observing that $\epsilon_4(\theta + \pi) = -\epsilon_4(\theta)$ and $\epsilon_5(\theta + \pi) = -\epsilon_5(\theta)$, it is obvious that $\lambda_1(\theta + \pi) = -\lambda_3(\theta)$. Consequently, $x_1(\theta + \pi) = x_3(\theta)$ and $y_1(\theta + \pi) = y_3(\theta)$. The first and third characteristic planes therefore obey the same equation and define the same characteristic surfaces. This is consistent with the properties of the bicharacteristic form of the two-dimensional shallow water equations [4, 7].

Characteristic surfaces. The second eigenvalue ($p = 2$) yields

$$\lambda_2 = (\epsilon_1 u + \epsilon_3 v)\cos\theta + \epsilon_2 v \sin\theta \tag{24a}$$

$$\partial_\theta \lambda_2 = -(\epsilon_1 u + \epsilon_3 v)\sin\theta + \epsilon_2 v \cos\theta \tag{24b}$$

$$\mathrm{d}_t \begin{bmatrix} x_2 \\ y_2 \end{bmatrix} = \begin{bmatrix} \epsilon_1 u + \epsilon_3 v \\ \epsilon_2 v \end{bmatrix} \tag{24c}$$

It reduces to a line in the (x, y, t) space.

The first and third characteristic surfaces form a cone with an elliptic-like base curve. The curve expands from the point (x_2, y_2) at a speed $\left(\epsilon_4^2 + \epsilon_5^2\right)^{\frac{1}{2}} c$ in the direction that makes an angle θ with the $x-$axis:

$$\lambda_3 = \lambda_2 + \left(\epsilon_4^2 + \epsilon_5^2\right)^{\frac{1}{2}} c \tag{25a}$$

$$\partial_\theta \lambda_3 = \partial_\theta \lambda_2 + \partial_\theta \left(\epsilon_4^2 + \epsilon_5^2\right)^{\frac{1}{2}} c \tag{25b}$$

$$\mathrm{d}_t \begin{bmatrix} x_3 \\ y_3 \end{bmatrix} = \begin{bmatrix} x_2 \\ y_2 \end{bmatrix} + \begin{bmatrix} \cos\theta & -\sin\theta \\ \sin\theta & \cos\theta \end{bmatrix} \begin{bmatrix} \left(\epsilon_4^2 + \epsilon_5^2\right)^{\frac{1}{2}} c \\ \partial_\theta \left(\epsilon_4^2 + \epsilon_5^2\right)^{\frac{1}{2}} c \end{bmatrix} \tag{25c}$$

The minimum and maximum extensions from the second characteristic surfaces are found in the directions θ_0 such that $\epsilon_4^2 + \epsilon_5^2$ is minimum/maximum. θ_0 is given by (see the Appendix, Subsec-

tion A.1.4):

$$\theta_0 = \frac{1}{2}\tan^{-1}\left(2\frac{\epsilon_2\epsilon_3}{\epsilon_1^2-\epsilon_2^2+\epsilon_3^2}\right) + k\frac{\pi}{2} \tag{26}$$

Particular case: orthogonal principal directions. This corresponds to $\alpha = 0$, then $\epsilon_3 = 0$ and

$$\theta_0 = k\pi/2 \tag{27a}$$

$$\theta_0 = k\pi \Rightarrow \left(\epsilon_4^2+\epsilon_5^2\right)^{\frac{1}{2}} c = \epsilon_1 c \tag{27b}$$

$$\theta_0 = \frac{\pi}{2} + k\pi \Rightarrow \left(\epsilon_4^2+\epsilon_5^2\right)^{\frac{1}{2}} c = \epsilon_2 c \tag{27c}$$

This is consistent with the wave speeds found in [15].

3.3 Analysis of the DIP model

Tangent planes. The differential conservation form for the DIP model [12] can be written in the form (20a) by defining the flux tensor as (see Appendix A.2 for a proof)

$$\mathbf{F} = \begin{bmatrix} q & r \\ \frac{1}{\epsilon_1}\frac{q^2}{h} + \epsilon_6\frac{qr}{h} + \epsilon_1\frac{g}{2}h^2 & \frac{1}{\epsilon_2}\frac{qr}{h} \\ \frac{1}{\epsilon_1}\frac{qr}{h} + \epsilon_6\frac{r^2}{h} + \epsilon_3\frac{g}{2}h^2 & \frac{1}{\epsilon_2}\frac{r^2}{h} + \epsilon_2\frac{g}{2}h^2 \end{bmatrix} \tag{28a}$$

$$\epsilon_6 = \left(\frac{1}{\epsilon_1} - \frac{1}{\epsilon_2}\right)\tan\alpha \tag{28b}$$

The expression for the matrix $\mathbf{A}_\theta$ is then (see Section A.2.3 in the Appendix for the details):

$$\mathbf{A}_\theta = \begin{bmatrix} 0 & \cos\theta & \sin\theta \\ \epsilon_4 c^2 - \epsilon_7 u^2 - \epsilon_8 uv & 2\epsilon_7 u + \epsilon_8 v & \epsilon_8 u \\ \epsilon_5 c^2 - \epsilon_7 uv - \epsilon_8 v^2 & \epsilon_7 v & \epsilon_7 u + 2\epsilon_8 v \end{bmatrix} \tag{29}$$

$$\epsilon_7 = \frac{\cos\theta}{\epsilon_1}, \quad \epsilon_8 = \epsilon_6\cos\theta + \frac{\sin\theta}{\epsilon_2} \tag{30}$$

So far, no analytical expression has been found for the eigenvalues of the matrix $\mathbf{A}_\theta$ in the general case. Numerical experiments show that, for arbitrary combinations$(\phi_1, \phi_2, \alpha, \theta)$, $\epsilon_7 u + \epsilon_8 v$ is not an eigenvalue of $\mathbf{A}_\theta$ if $(u, v) \neq (0, 0)$. Since the trace of the matrix is $3\left(\epsilon_7 u + \epsilon_8 v\right)$, this means that $\lambda_1 + \lambda_3 \neq 2\lambda_2$. This has consequences on the shape of the second bicharacteristic surface, as seen in the next paragraph.

A particular case arises for $u = v = 0$. This is is the configuration of the test presented in Section 2.1. In this case, $\det \mathbf{A}_\theta = \mathrm{tr}\mathbf{A}_\theta = 0$ and analytical expressions are available for the eigenvalues of $\mathbf{A}_\theta$:

$$\lambda_p = (p-2)\left(\epsilon_1\cos^2\theta + \epsilon_2\sin^2\theta + \epsilon_3\cos\theta\sin\theta\right)^{\frac{1}{2}} \tag{31}$$

Characteristic surfaces. No general, analytical expression having been found so far for the eigenvalues, the characteristic surfaces are determined by solving the characteristic polynomial numerically (see A.3 in the Appendix for the procedure). It is observed that, in the general

case, $2\lambda_2 \neq \lambda_1 + \lambda_3$ (see the above paragraph). Consequently, the first and third characteristic surfaces do not extend symmetrically from the second one as with the IP model. Besides, numerical experiments indicate that in the general case the second characteristic surface does not reduce to a line as in the IP model (see Section 4).

For the particular case $u = v = 0$, the analytical solution (58) yields

$$\partial_\theta \lambda_p = (p-2)\,\frac{(\epsilon_2 - \epsilon_1)\sin 2\theta + \epsilon_3 \cos 2\theta}{2\lambda_p} \tag{32}$$

$$\mathrm{d}_t \begin{bmatrix} x_p \\ y_p \end{bmatrix} = (p-2) \begin{bmatrix} \cos\theta & -\sin\theta \\ \sin\theta & \cos\theta \end{bmatrix} \begin{bmatrix} \left(\epsilon_1 \cos^2\theta + \epsilon_2 \sin^2\theta + \epsilon_3 \cos\theta \sin\theta\right)^{\frac{1}{2}} \\ \frac{(\epsilon_2-\epsilon_1)\sin 2\theta + \epsilon_3 \cos 2\theta}{2\left(\epsilon_1 \cos^2\theta + \epsilon_2 \sin^2\theta + \epsilon_3 \cos\theta \sin\theta\right)^{\frac{1}{2}}} \end{bmatrix} \tag{33}$$

The directions of minimum and maximum extensions are found for θ_0 such that $\partial_\theta \lambda_p(\theta_0) = 0$, that is

$$(\epsilon_1 - \epsilon_2)\sin 2\theta - \epsilon_3 \cos\theta = 0 \tag{34a}$$

$$\tan 2\theta_0 = \frac{\epsilon_3}{\epsilon_1 - \epsilon_2} \tag{34b}$$

$$\theta_0 = \frac{1}{2}\tan^{-1}\left(\frac{\epsilon_3}{\epsilon_1 - \epsilon_2}\right) + k\frac{\pi}{2} \tag{34c}$$

This formula is different from that of the IP model (26).

4 Computational examples

4.1 Initial Value Problems

The purpose of the present section is to show that the bicharacteristic analysis presented in Section 3 allows the features of the solution of the IP and DIP equations to be fully characterized. The influence of the mesh design is illustrated for Initial Value Problems (IVPs) with the following initial conditions

$$h(x,y,0) = \begin{cases} h_0 & \text{for} \quad |x| < d,\ |y| < d \\ h_1 & \text{otherwise} \end{cases} \tag{35a}$$

$$\mathbf{q}(x,y,0) = [hu_0, 0]^T \ \forall (x,y) \tag{35b}$$

The water is initially moving at a uniform speed u_0. The water depth is piecewise constant, uniformly equal to h_0, except in a square region of size d where it is equal to h_1. The IP and DIP equations are solved numerically using mesh Designs 1, 2 and 3 presented in Subsection 2.2. The parameter values are summarized in Table 2. It is reminded that Figure 6 must be applied a 90 degree rotation to retrieve Design 2. This rotation is applied to all the computational results in what follows. With this convention, the $x-$ and $y-$axes point to the South and East respectively. The computational results are plotted in the form of filled contour maps for a simulation time T such that the waves stemming from the IVP do not reach the boundaries of the numerical domain yet. The coordinates (x_p, y_p) for the IP and DIP models are plotted for the same time.

Symbol	Meaning	Numerical value
d	Size of the square domain	20 m
g	Gravitational acceleration	$9.81\,\mathrm{ms}^{-2}$
h_0	Initial water depth in the infinite domain	1 m
h_1	Initial water depth in the square region $d \times d$	1.1 m
T	Simulated time	150 s
ϕ	Domain porosity	$\frac{7}{9}$

Table 2: Parameter sets for the computational examples.

4.2 Isotropic case with water initially at rest

In this case the porosity is isotropic, $\phi_1 = \phi_2 = 2/3$ and the water is initially at rest everywhere in the domain. According to the consistency analysis in Section 2, the governing equations are isotropic for all mesh designs. The numerical solutions are therefore expected to be almost isotropic, with a slight anisotropy induced by the numerical diffusion arising from second-order truncation errors. The wave speed formulae (25a, 31) yield larger wave speeds for the DIP model than for the IP model.

Figure 8 shows the water depth maps computed at $t = 150$s for the three mesh designs. The top graphs are the outputs obtained by running the IP model while the bottom maps are obtained from the DIP model. The characteristic surfaces are also plotted in Figures 8a-f. Note that the first and third surfaces are identical, while the second surface reduces to a point located at the centre of the first/third surface. The bicharacteristic surface is seen to superimpose well with the contour lines of the numerical results. The slight anisotropy observed in the numerical contours can be explained by numerical diffusion. Numerical diffusion also explains that the contour lines expand faster than the characteristic surfaces.

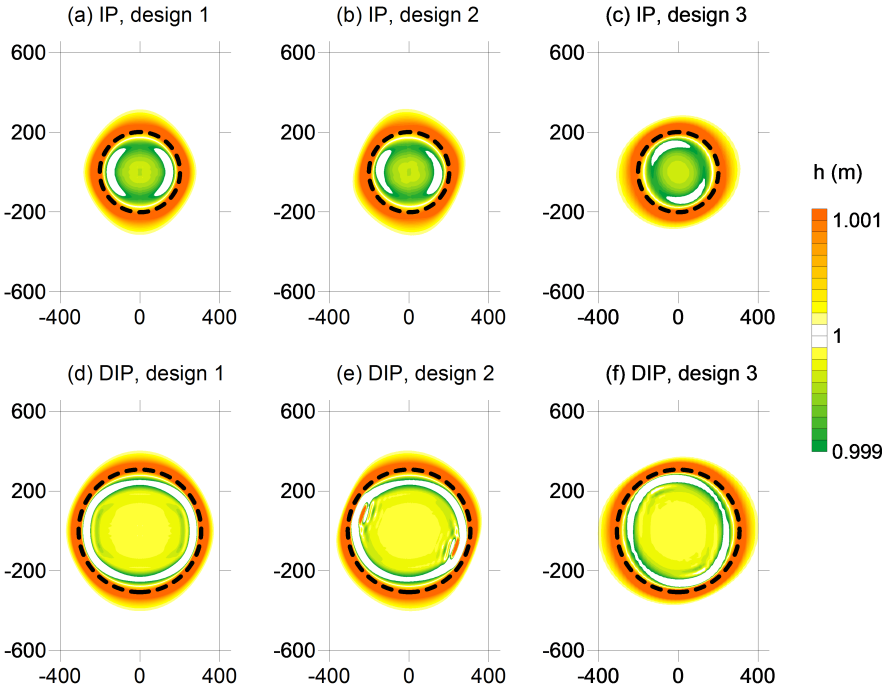

Figure 8: Isotropic IVP with water at rest. Contour map: water depth computed at t =150s. Dashed line: first and third characteristic surfaces. $x-$ and $y-$ coordinates in metres.

4.3 Anisotropic case with water initially at rest

In this case the porosity is anisotropic, with $\phi_1 = 2/3$ and $\phi_2 = 1/3$. The initial flow velocity is set to $u_0 = 0$. The waves therefore expand symmetrically from the centre $(0, 0)$. Figure 9 represent the water depths computed by the two models for the three mesh designs at $t = 150$s. The dashed lines in Figs. 9a, 9b, 9d and 9f represent the first and third bicharacteristics as computed from the theoretical formulae (25a, 25b, 25c) and (31, 33). No bicharacteristic surface is provided for mesh design 3 because the expressions derived in Section 3 are not applicable to the triangular mesh. As expected from the analysis in Section 3, the first and third families are identical. The second family again reduces to the point $(0, 0)$ and is not represented in the figures.

As expected from Sections 2 and 3, the influence of the mesh design on the numerical solution is clearly visible. A non-orthogonal mesh (Designs 2 and 3) contributes to apply a shear distortion to the numerical solution. This was expected from the theoretical bicharacteristic formulae, that match match very precisely the numerical solution, both in terms of extension in the $x-$ and $y-$directions and in terms of mesh-induced directional bias. This serves as a confirmation that the DIP formulae (31, 33), albeit derived for a particular case, are valid. The flux polarization along the $y-$axis, that was expected from Subsection 2.3, is particularly visible in Figure 9c (IP model results), with stronger depth variations in the $y-$direction than in the $x-$direction. This effect is less apparent in Figure 9f (DIP model results). This can easily be explained by the differential form of the DIP continuity equation (55). In contrast with the IP continuity equation, the DIP continuity equation is isotropic. Flux polarisation is thus minimized.

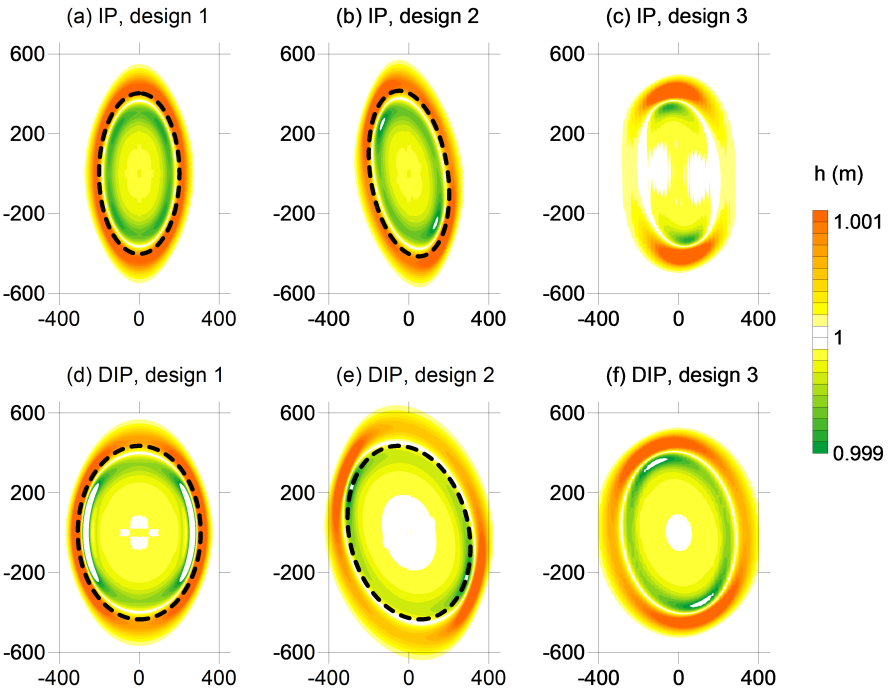

Figure 9: Anisotropic IVP with water at rest. Contour map: water depth computed at t =150s. Dashed line: first and third bicharacteristic surfaces. $x-$ and $y-$ coordinates in metres.

4.4 Anisotropic case with initial velocity

In this case the porosity configuration is the same as in the previous subsection. The initial flow velocity is set to $u_0 = 1\text{ms}^{-1}$. With the 90 degrees clockwise rotation of the coordinate system, this corresponds to a velocity directed to the South. While formulae (24a, 25a) for the IP model remain valid, equation (31) cannot be used for the DIP model and the eigenvalues must be found numerically. The second eigenvalue for the DIP model is not equal to the average of the first and third one and the second characteristic surface does not reduce to a line.

The numerical solutions at $t = 150$s for the three mesh designs and the two models are shown in Figure 10. The theoretical characteristic surfaces are superimposed with the numerical fields for mesh designs 1 and 2. As in the previous test case, the effects of the mesh bias on the numerical solutions is clearly visible. This effect can again be explained by the bicharacteristic analysis, with theoretical characteristic surfaces matching very closely the contour lines of the numerical solutions.

A first striking feature of the DIP solution (as opposed to the IP solution) is its asymmetrical character in the longitudinal direction. A second noticeable feature is that the second characteristic surface does not reduce to a line as in the shallow water and IP model equations. In the case of mesh Design 3, the effects of flux polarization along the N-S direction is again visible, albeit milder in the DIP solution than in the IP solution.

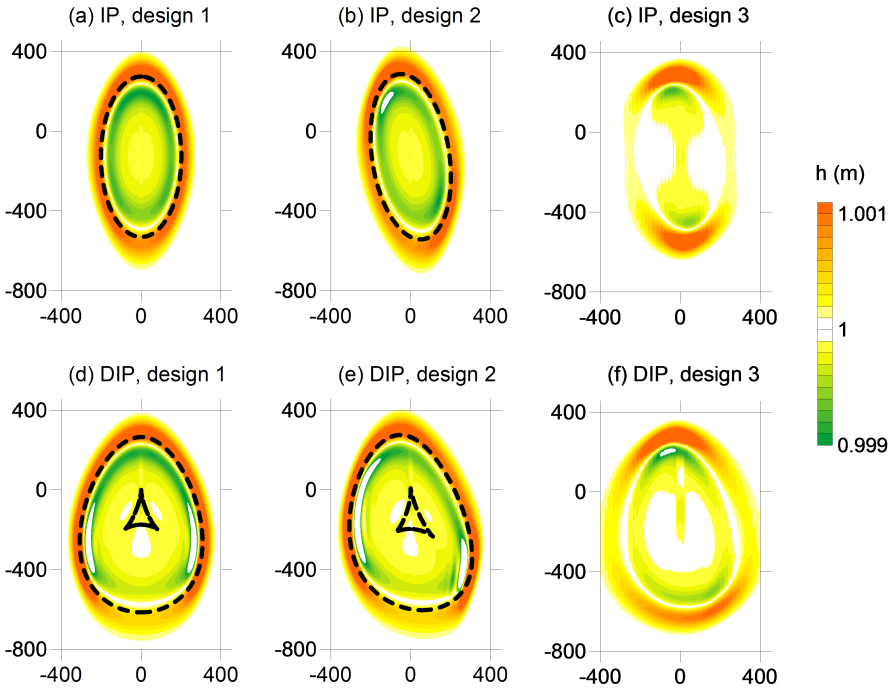

Figure 10: Anisotropic IVP with initial velocity. Contour map: water depth computed at t =150s. Dashed line: characteristic surfaces. $x-$ and $y-$ coordinates in metres.

4.5 Anisotropic case: influence of rectangular mesh orientation

The purpose of this test is to assess the consequences of changing the principal directions of a rectangular mesh on the numerical wave propagation speeds. This test is of practical interest because recently published depth-dependent IP models [16, 17] use structured, Cartesian grids. A Cartesian grid is most unlikely to coincide with the principal directions of the street network in all parts of a city. Consequently, it is important to assess the influence of a Cartesian grid not aligned with the principal directions of the urban layout. The building layout of Subsection 2.2 (Figure 1) is used, with the building size and spacing given in Table 1. The mesh is rectangular and makes an angle β with the $x-$axis. There are four mesh designs where a rectangular mesh encompassing one $x-$period yields a homogeneous porosity field: Design 1 shown on Figure 2, and Designs 4-6 shown on Figure 11. The corresponding angles β and the conveyance porosities along the principal directions of the mesh are given in Table 4. The strongest bias is found for $\beta = \frac{\pi}{4}$. In this case, the apparent connectivity porosity field is fully isotropic.

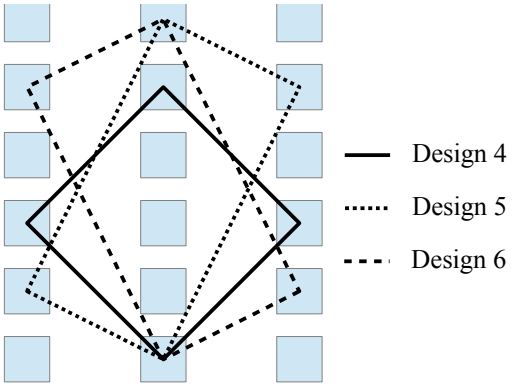

Figure 11: Anisotropic IVP with rectangular meshes. Mesh designs 4 to 6.

Mesh design	β	ϕ_1	ϕ_2
1	0	$\frac{1}{3}$	$\frac{2}{3}$
4	$\frac{\pi}{4}$	$\frac{2}{3}$	$\frac{2}{3}$
5	$\tan^{-1} 2$	$\frac{2}{3}$	$\frac{3}{4}$
6	$\tan^{-1} 2 + \frac{\pi}{2}$	$\frac{2}{3}$	$\frac{3}{4}$

Table 3: Parameters for mesh designs 4-6. β is the angle between the $x-$axis and the first principal direction of the mesh, ϕ_1 and ϕ_2 are respectively the connectivity porosities along the first and second principal directions of the mesh.

The IVP is the same as that of Subsection 4.3 (water initially at rest). Figure 12 shows the first and third characteristic surfaces at $t = 200$s for Designs 1, 4, 5 and 6. The second characteristic reduces to the point $(0, 0)$. The characteristic surfaces for a given model (IP and DIP) are shown on the same graph for an easier comparison of the four mesh designs. The computed water depth fields are not shown for the sake of clarity. While the characteristic surfaces obtained from Designs 4-6 are close to each other, they depart significantly, from the solution obtained from Design 1. This is true for both the IP and IVP model. Overall, however, the DIP model (Figure 12, right) is less sensitive to the angle β than is the IP model (Figure 12, left). It is also worth noting that all four designs lead to the same maximum wave speed along the $y-$direction.

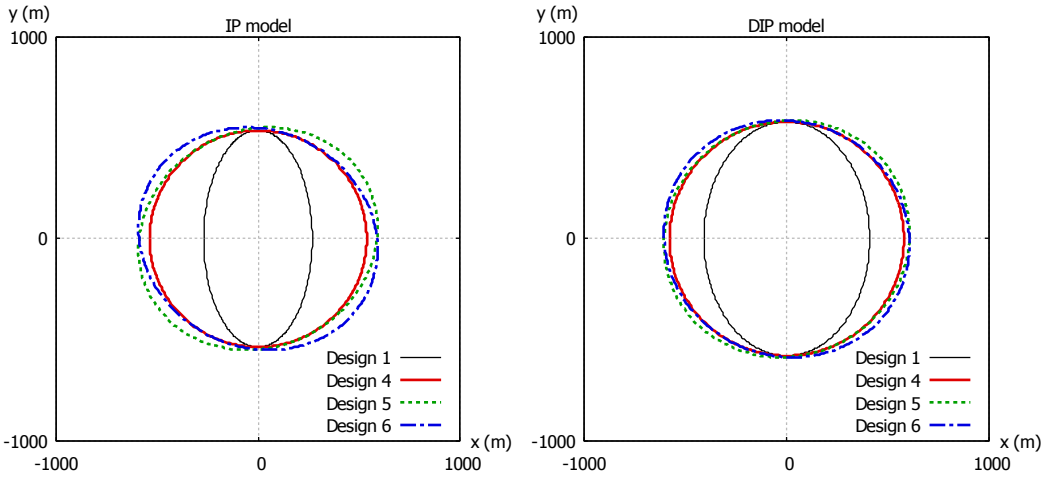

Figure 12: Anisotropic IVP with rectangular meshes. First and third characteristic surfaces at $t = 200$s. The second characteristic surface is the point $(0, 0)$.

5 Conclusions

A consistency and two-dimensional characteristic analysis is carried out in Sections 2-3 for the two-dimensional IP and DIP models. The analysis deals with idealized situations where the porosity parameters fields are uniform and the mesh is periodic. It focuses on the conservation part of the equations. The momentum source terms accounting for the effects of bottom friction, bottom slope and drag-induced momentum and energy dissipation terms are not considered in the analysis. They can be expected to reduce the amount of error induced by the consistency issues raised in he present paper. However, in the absence of analytical solutions for the IP/DIP equations with bottom and friction source terms, the influence of the source terms on consistency error damping is difficult to assess.

As far as the hyperbolic part of the IP and DIP models is concerned, the main conclusions are the following.

(a) The sensitivity of the models to the mesh design is minimum when the connectivity porosity ϕ_Γ is isotropic (that is, identical for all the edges of a given computational cell). This explains why the SP and MP models, that use identical ϕ_Γ and ϕ_Ω, are almost insensitive to the mesh design.

(b) Defining a non-uniform connectivity porosity ϕ_Γ over the cell boundary induces an artificial polarization of the mass and/or momentum fluxes in the direction orthogonal to the vector $\int_\Gamma \phi_\Gamma \mathbf{n} d\Gamma$. Such adverse effects can be avoided by making the integral $\int_\Gamma \phi_\Gamma \mathbf{n} d\Gamma$ zero. This, however, implies that the porosity ϕ_Γ cannot be derived only from the urban geometry as done in all previous applications of integral porosity models [12, 14, 18]. It must be fine-tuned in all the cells so as to fulfil the constraint (10).

(c) Assuming that the polarization bias (b) has been eliminated by enforcing the condition (10) in all the cells, another bias arises from cell edge orientation. The consistency and characteristic analyses in Sections 2-3 show that the wave propagation principal directions are functions of the angle between the cell edges.

The analysis is validated in Section 4 by verifying the theoretical characteristic surfaces against numerical solutions of the IP and DIP models. The theoretical analysis of Sections 2-3 allows the behaviour of the numerical solution and the influence of the discretization bias to be predicted with excellent accuracy. The DIP model is also shown to be significantly less sensitive to the grid than is the IP model. This is attributed to the fact that the connectivity porosity is involved in all three equations of the IP model, while it is not involved in the continuity equation of the DIP model.

Should mesh design guidelines be provided to the modeller using an integral porosity model, they would be the following.

(d) In regions where the porosity ϕ_Γ is anisotropic, the mesh should be designed in such a way that the orientations of the cell edges are distributed as uniformly as possible over all possible directions of space (as in [19]). Doing so allows the condition (10) to be satisfied without inducing a strong flux polarization as in mesh Design 3. When the porosity ϕ_Γ is isotropic, preferential directions in the cell edge orientation are acceptable.

(e) If rectangular cells are used over an orthogonal street network, the cell edges should be aligned with the principal directions of the street network. Orienting rectangular cells along different directions or shearing the cells in a given direction will alter the magnitude and the principal directions of the wave propagation speeds.

In the field of hydrological modelling, using the consistency properties and the truncation error of a discretization to reconstruct the influence of physical parameters has long been customary practice (see e.g. [3] for a well-known example). But doing so implies that the modeller is well-aware of the consistency properties of the model. It also implies that the effects of the truncation error are easily controllable by the modeller. In the example [3], the truncation error acts mostly on second-order space derivatives, which brings marginal modification to the model propagation properties (albeit raising issues in terms of boundary conditions). In the case of the IP and DIP models, the consequences are much stronger. If the condition (10) is fulfilled, the consistency bias (c) acts on the first-order space derivatives, thus modifying the properties of the hyperbolic system. If equation (10) is not satisfied, the consistency bias (b) introduces null-order derivatives in the truncation error, which is the strongest possible bias in a system of partial differential equations.

From a practical point of view, hydraulic modelling engineers and technicians cannot be expected to run a consistency and bicharacteristic analysis for each cell in the mesh. Besides, removing the consistency bias (b) is a non-local operation: enforcing condition (10) in a given cell can be achieved only by modifying ϕ_Γ over one or several cell interfaces. Since an interface belongs to two cells (with the exception of boundaries), the change in ϕ_Γ will also affect the neighbouring cell. Adjustments to the connectivity porosity are thus liable to propagate from cell to cell. In practical applications, this can be done only using automated procedures. But it is not certain that (i) the resulting, adjusted ϕ_Γ field will be independent from the starting interface of the adjustments, (ii) the adjusted field will be physically acceptable to the hydraulic engineer. Complying with recommendations (d-e) thus appears to be the easiest and most reliable way of eliminating the consistency bias.

Although integral porosity models are clearly more accurate than single porosity models, the present study shows that they still have shortcomings. While the DIP model is clearly superior to the IP model in terms of sensitivity to mesh design, it is believed that mesh dependency can be reduced further. This might be achieved by providing a better description of the connectivity

porosity field via appropriate flux closure models. This calls for complementing the building footprint approach, that is a point-based assessment of the connectivity porosity ϕ_Γ, with an approach that better reflects the connectivity properties of the urban medium within the cells and not only at the cell interfaces. Such an approach is yet to be proposed.

Acknowledgements

The author is extremely grateful to the Associate Editor and the two reviewers for their constructive comments and suggestions. More specifically, Prof. B.F. Sanders pointed out the mesh design strategy in [19] as an example of successful minimization of the consistency bias. The test in Subsection 4.5 was developed following a suggestion of the anonymous Reviewer 2.

Appendix. Proofs and algorithmic details

A.1 IP model governing equations

The differential form for the governing equations of the IP model is obtained by applying the integral formulae to the quadrangular cell shown in Figure 6.

A.1.1 Continuity equation

The continuity equation is

$$\partial_t \int_\Omega \phi h \,\mathrm{d}\Omega + \int_\Gamma \phi_\Gamma \mathbf{q}_\Gamma.\mathbf{n} \,\mathrm{d}\Gamma = 0 \tag{36}$$

with the closure model $\mathbf{q}_\Gamma = \mathbf{q}$. First-order Taylor series expansions with the distribution of ϕ_Γ of Figure 6 give

$$\int_\Omega \phi h \,\mathrm{d}\Omega = \mathrm{d}x\mathrm{d}y\phi h \tag{37a}$$

$$\begin{aligned}
\textstyle\int_\Gamma \phi_\Gamma \mathbf{q}_\Gamma.\mathbf{n} \,\mathrm{d}\Gamma &= \textstyle\int_\Gamma \phi_\Gamma \mathbf{q}.\mathbf{n} \,\mathrm{d}\Gamma \\
&= \tfrac{\mathrm{d}y}{\cos\alpha} \left(\phi_1 q \cos\alpha + \phi_1 r \sin\alpha\right)_{x+\frac{\mathrm{d}x}{2},y} \\
&\quad - \tfrac{\mathrm{d}y}{\cos\alpha} \left(\phi_1 q \cos\alpha + \phi_1 r \sin\alpha\right)_{x-\frac{\mathrm{d}x}{2},y} \\
&\quad + \mathrm{d}x \left(\phi_2 r\right)_{x-\frac{\mathrm{d}y}{2}\tan\alpha, y+\frac{\mathrm{d}y}{2}} - \mathrm{d}x \left(\phi_2 r\right)_{x+\frac{\mathrm{d}y}{2}\tan\alpha, y-\frac{\mathrm{d}y}{2}} \\
&= \mathrm{d}x\mathrm{d}y \left[\partial_x \left(\phi_1 q + \left(\phi_1 - \phi_2\right)\tan\alpha r\right) + \partial_y \left(\phi_2 r\right)\right]
\end{aligned} \tag{37b}$$

hence, after simplifying by $\mathrm{d}x\mathrm{d}y\phi$:

$$\partial_t h + \partial_x \left(\frac{\phi_1}{\phi} q + \frac{\phi_1 - \phi_2}{\phi} \tan\alpha r\right) + \partial_y \left(\frac{\phi_2}{\phi} r\right) = 0 \tag{38}$$

A.1.2 Momentum equations

Vector form. The vector form is

$$\partial_t \int_\Omega \phi h \mathbf{u} \,\mathrm{d}\Omega + \int_\Gamma \phi_\Gamma \left[\left(\mathbf{q}_\Gamma.\mathbf{n}\right)\mathbf{u}_\Gamma + \frac{g}{2} h^2 \mathbf{n}\right] \mathrm{d}\Gamma = 0 \tag{39}$$

The first integral is

$$\int_\Omega \phi h \mathbf{u} \,\mathrm{d}\Omega = \mathrm{d}x\mathrm{d}y\phi h\mathbf{u} \tag{40}$$

while the closure relationship $\mathbf{q}_\Gamma = \mathbf{q}$ leads to

$$\int_\Gamma \phi_\Gamma \left[(\mathbf{q}_\Gamma.\mathbf{n})\, \mathbf{u}_\Gamma + \frac{g}{2} h^2 \mathbf{n} \right] \mathrm{d}\Gamma = \int_\Gamma \phi_\Gamma \left[(\mathbf{q}.\mathbf{n})\, \mathbf{u} + \frac{g}{2} h^2 \mathbf{n} \right] \mathrm{d}\Gamma \tag{41}$$

x-momentum flux. Projecting the integral (41) onto the $x-$axis with $\mathbf{q} = [q, r]^T$ and $\mathbf{n} = [n_x, n_y]^T$ gives

$$\begin{aligned} m_x &= \int_\Gamma \left[\phi_\Gamma \left(\mathbf{q}.\mathbf{n} \right) \tfrac{q}{h} + \tfrac{g}{2} h^2 n_x \right] \mathrm{d}\Gamma \\ &= \tfrac{\mathrm{d}y}{\cos\alpha} \left[\phi_1 \left(\tfrac{q^2}{h} \cos\alpha + \tfrac{qr}{h} \sin\alpha + \tfrac{g}{2} h^2 \cos\alpha \right) \right]_{x+\frac{\mathrm{d}x}{2}, y} () \\ &\quad - \tfrac{\mathrm{d}y}{\cos\alpha} \phi_1 \left[\tfrac{q^2}{h} \cos\alpha + \tfrac{qr}{h} \sin\alpha + \tfrac{g}{2} h^2 \cos\alpha \right]_{x-\frac{\mathrm{d}x}{2}, y} \\ &\quad + \phi_2 \mathrm{d}x \left[\left(\tfrac{qr}{h} \right)_{x-\frac{\mathrm{d}y}{2}\tan\alpha, y+\frac{\mathrm{d}y}{2}} - \left(\tfrac{qr}{h} \right)_{x+\frac{\mathrm{d}y}{2}\tan\alpha, y-\frac{\mathrm{d}y}{2}} \right] \\ &= \mathrm{d}x\mathrm{d}y \left[\partial_x \left(\phi_1 \tfrac{q^2}{h} + (\phi_1 - \phi_2) \tan\alpha \partial_x \tfrac{qr}{h} + \phi_1 \tfrac{g}{2} h^2 \right) + \partial_y \left(\phi_2 \tfrac{qr}{h} \right) \right] \end{aligned} \tag{42}$$

hence the $x-$momentum equation

$$\partial_t q + \partial_x \left(\frac{\phi_1}{\phi} \frac{q^2}{h} + \frac{\phi_1 - \phi_2}{\phi} \tan\alpha \partial_x \frac{qr}{h} + \frac{\phi_1}{\phi} \frac{g}{2} h^2 \right) + \partial_y \left(\frac{\phi_2}{\phi} \frac{qr}{h} \right) = 0 \tag{43}$$

y-momentum flux. Projecting the integral (41) onto the $y-$axis gives

$$\begin{aligned} m_y &= \int_\Gamma \left[\phi_\Gamma \left(\mathbf{q}.\mathbf{n} \right) \tfrac{r}{h} + \tfrac{g}{2} h^2 n_y \right] \mathrm{d}\Gamma \\ &= \tfrac{\mathrm{d}y}{\cos\alpha} \left[\phi_1 \left(\tfrac{qr}{h} \cos\alpha + \tfrac{r^2}{h} \sin\alpha + \tfrac{g}{2} h^2 \sin\alpha \right) \right]_{x+\frac{\mathrm{d}x}{2}, y} \\ &\quad - \phi \tfrac{\mathrm{d}y}{\cos\alpha} \left[\phi_1 \left(\tfrac{qr}{h} \cos\alpha + \tfrac{r^2}{h} \sin\alpha + \tfrac{g}{2} h^2 \sin\alpha \right) \right]_{x-\frac{\mathrm{d}x}{2}, y} \\ &\quad + \mathrm{d}x \left[\phi_2 \left(\tfrac{r^2}{h} + \tfrac{g}{2} h^2 \right) \right]_{x-\frac{\mathrm{d}y}{2}\tan\alpha, y+\frac{\mathrm{d}y}{2}} - \mathrm{d}x \left[\phi_2 \left(\tfrac{r^2}{h} + \tfrac{g}{2} h^2 \right) \right]_{x+\frac{\mathrm{d}y}{2}\tan\alpha, y-\frac{\mathrm{d}y}{2}} \\ &= \mathrm{d}x\mathrm{d}y\partial_x \left[\phi_1 \tfrac{qr}{h} + (\phi_1 - \phi_2) \tan\alpha \tfrac{r^2}{h} + (\phi_1 - \phi_2) \tan\alpha \tfrac{g}{2} h^2 \right] + \mathrm{d}x\mathrm{d}y\partial_y \left[\phi_2 \left(\tfrac{r^2}{h} + \tfrac{g}{2} h^2 \right) \right] \end{aligned} \tag{44}$$

hence the $y-$momentum equation

$$\partial_t r + \partial_x \left[\frac{\phi_1}{\phi} \frac{qr}{h} + \left(\frac{\phi_1 - \phi_2}{\phi} \right) \tan\alpha \frac{r^2}{h} + \frac{(\phi_1 - \phi_2) \tan\alpha}{\phi} \frac{g}{2} h^2 \right] + \partial_y \left[\frac{\phi_2}{\phi} \left(\frac{r^2}{h} + \frac{g}{2} h^2 \right) \right] = 0 \tag{45}$$

A.1.3 Jacobian matrices

The Jacobian matrices $\mathbf{A}_x$ and $\mathbf{A}_y$ are obtained by differentiating the flux tensor obtained from equations (38, 43, 45) with respect to the conserved variable:

$$\mathbf{A}_x = \begin{bmatrix} 0 & \epsilon_1 & \epsilon_3 \\ \left(c^2 - u^2\right) \epsilon_1 - \epsilon_3 uv & 2\epsilon_1 u + \epsilon_3 v & \epsilon_3 u \\ \left(c^2 - v^2\right) \epsilon_3 - \epsilon_1 uv & \epsilon_1 v & 2\epsilon_3 v + \epsilon_1 u \end{bmatrix} \tag{46}$$

$$\mathbf{A}_y = \begin{bmatrix} 0 & 0 & \epsilon_2 \\ -\epsilon_2 uv & \epsilon_2 v & \epsilon_2 u \\ \epsilon_2 \left(c^2 - v^2\right) & 0 & 2\epsilon_2 v \end{bmatrix} \tag{47}$$

The resulting expression for $\mathbf{A}_\theta$ in equation (21a) follows directly from equation (18).

A.1.4 Principal directions of the first and third characteristic surfaces

The directions of minimum/maximum extensions of the two characteristic surfaces are those for which

$$\partial_\theta \left(\lambda_3 - \lambda_1\right) = 0 \tag{48}$$

This leads to the condition

$$\epsilon_4 \partial_\theta \epsilon_4 + \epsilon_5 \partial_\theta \epsilon_5 = 0 \tag{49}$$

Consequently

$$\epsilon_2 \epsilon_3 \cos 2\theta_0 = \frac{1}{2}\left(\epsilon_1^2 - \epsilon_2^2 + \epsilon_3^2\right) \sin 2\theta_0 \tag{50a}$$

$$\tan 2\theta_0 = 2\frac{\epsilon_2 \epsilon_3}{\epsilon_1^2 - \epsilon_2^2 + \epsilon_3^2} \tag{50b}$$

which leads to equation (26). The directions of the minimum and maximum expansion speeds are thus orthogonal. Then, from equation (50b)

$$\left(\epsilon_4^2 + \epsilon_5^2\right)^{\frac{1}{2}} c = \left[\cos 2\theta_0 \left(\frac{\epsilon_1^2 - \epsilon_2^2 + \epsilon_3^2}{2} + 2\frac{\epsilon_2^2 \epsilon_3^2}{\epsilon_1^2 - \epsilon_2^2 + \epsilon_3^2}\right) + \frac{\epsilon_1^2 + \epsilon_2^2 + \epsilon_3^2}{2}\right]^{1/2} c \tag{51}$$

and

$$\begin{bmatrix} \cos\theta & -\sin\theta \\ \sin\theta & \cos\theta \end{bmatrix} \begin{bmatrix} \lambda_p \\ \partial_\theta \lambda_p \end{bmatrix} = \begin{bmatrix} \cos\theta_0 & -\sin\theta_0 \\ \sin\theta_0 & \cos\theta_0 \end{bmatrix} \begin{bmatrix} \left(\epsilon_4^2 + \epsilon_5^2\right)^{\frac{1}{2}} c \\ 0 \end{bmatrix} = \begin{bmatrix} \cos\theta_0 \\ \sin\theta_0 \end{bmatrix} \left(\epsilon_4^2 + \epsilon_5^2\right)^{\frac{1}{2}} c \tag{52}$$

A.2 DIP model governing equations

The differential form for the governing equations of the DIP model is obtained by applying the integral formulae to the quadrangular cell shown in Figure 6.

A.2.1 Continuity equation.

The continuity equation is

$$\partial_t \int_\Omega \phi h \,\mathrm{d}\Omega + \int_\Gamma \phi_\Gamma \mathbf{q}_\Gamma . \mathbf{n} \,\mathrm{d}\Gamma = 0 \tag{53}$$

with the closure model $\mathbf{q}_\Gamma = \frac{\phi}{\phi_\Gamma}\mathbf{q}$. First-order Taylor series expansions give

$$\int_\Omega \phi h \,\mathrm{d}\Omega = \mathrm{d}x\mathrm{d}y \phi h \tag{54a}$$

$$\int_\Gamma \phi_\Gamma \mathbf{q}_\Gamma . \mathbf{n} \,\mathrm{d}\Gamma = \int_\Gamma \phi \mathbf{q} . \mathbf{n} \,\mathrm{d}\Gamma = \mathrm{d}x\mathrm{d}y \phi \left(\partial_x q + \partial_y r\right) \tag{54b}$$

hence, after simplifying by $\mathrm{d}x\mathrm{d}y\phi$:

$$\partial_t h + \partial_x q + \partial_y r = 0 \tag{55}$$

which is the same equation as that of the SP and Defina's models.

A.2.2 Momentum equations

Vector form. The vector form is

$$\partial_t \int_\Omega \phi h \mathbf{u}\, \mathrm{d}\Omega + \int_\Gamma \phi_\Gamma \left[(\mathbf{q}_\Gamma.\mathbf{n})\, \mathbf{u}_\Gamma + \frac{g}{2} h^2 \mathbf{n} \right] \mathrm{d}\Gamma = 0 \tag{56}$$

with $\mathbf{q} = h\mathbf{u}$. The first integral is

$$\int_\Omega \phi h \mathbf{u}\, \mathrm{d}\Omega = \mathrm{d}x\mathrm{d}y \phi h \mathbf{u} \tag{57}$$

while the closure relationship $\mathbf{q}_\Gamma = \frac{\phi}{\phi_\Gamma}\mathbf{q}$ leads to

$$\int_\Gamma \phi_\Gamma \left[(\mathbf{q}_\Gamma.\mathbf{n})\, \mathbf{u}_\Gamma + \frac{g}{2} h^2 \mathbf{n} \right] \mathrm{d}\Gamma = \phi \int_\Gamma \left[\frac{\phi}{\phi_\Gamma} (\mathbf{q}.\mathbf{n})\, \mathbf{u} + \frac{g}{2} \frac{\phi_\Gamma}{\phi} h^2 \mathbf{n} \right] \mathrm{d}\Gamma \tag{58}$$

x-momentum flux. Projecting the integral (58) onto the $x-$axis with $\mathbf{q} = [q, r]^T$ and $\mathbf{n} = [n_x, n_y]^T$ gives

$$\begin{aligned}
m_x &= \phi \textstyle\int_\Gamma \left[\frac{\phi}{\phi_\Gamma} (\mathbf{q}.\mathbf{n}) \frac{q}{h} + \frac{g}{2} \frac{\phi_\Gamma}{\phi} h^2 n_x \right] \mathrm{d}\Gamma \\
&= \phi \tfrac{\mathrm{d}y}{\cos\alpha} \left(\tfrac{\phi}{\phi_1} \cos\alpha \tfrac{q^2}{h} + \tfrac{\phi}{\phi_1} \sin\alpha \tfrac{qr}{h} + \tfrac{\phi_1}{\phi} \cos\alpha \tfrac{g}{2} h^2 \right)_{x+\frac{\mathrm{d}x}{2}, y} \\
&\quad - \phi \tfrac{\mathrm{d}y}{\cos\alpha} \left(\tfrac{\phi}{\phi_1} \cos\alpha \tfrac{q^2}{h} + \tfrac{\phi}{\phi_1} \sin\alpha \tfrac{qr}{h} + \tfrac{\phi_1}{\phi} \cos\alpha \tfrac{g}{2} h^2 \right)_{x-\frac{\mathrm{d}x}{2}, y} \\
&\quad + \phi \mathrm{d}x \left(\tfrac{\phi}{\phi_2} \tfrac{qr}{h} - \tfrac{\phi}{\phi_2} \tfrac{qr}{h} \right)_{x-\frac{\mathrm{d}y}{2}\tan\alpha, y+\frac{\mathrm{d}y}{2}} - \phi \mathrm{d}x \left(\tfrac{\phi}{\phi_2} \tfrac{qr}{h} - \tfrac{\phi}{\phi_2} \tfrac{qr}{h} \right)_{x+\frac{\mathrm{d}y}{2}\tan\alpha, y-\frac{\mathrm{d}y}{2}} \\
&= \phi \mathrm{d}x\mathrm{d}y \left[\tfrac{\phi}{\phi_1} \partial_x \tfrac{q^2}{h} + \left(\tfrac{\phi}{\phi_1} - \tfrac{\phi}{\phi_2} \right) \tan\alpha \partial_x \tfrac{qr}{h} + \tfrac{\phi_1}{\phi} \partial_x \tfrac{g}{2} h^2 + \tfrac{\phi}{\phi_2} \partial_y \tfrac{qr}{h} \right]
\end{aligned} \tag{59}$$

hence the $x-$momentum equation

$$\partial_t q + \partial_x \left[\frac{\phi}{\phi_1} \frac{q^2}{h} + \left(\frac{\phi}{\phi_1} - \frac{\phi}{\phi_2} \right) \tan\alpha \frac{qr}{h} + \frac{\phi_1}{\phi} \frac{g}{2} h^2 \right] + \partial_y \left(\frac{\phi}{\phi_2} \frac{qr}{h} \right) = 0 \tag{60}$$

y-momentum flux. Projecting the integral (58) onto the $y-$axis gives

$$\begin{aligned}
m_y &= \phi \textstyle\int_\Gamma \left[\frac{\phi}{\phi_\Gamma} (\mathbf{q}.\mathbf{n})\, v + \frac{g}{2} \frac{\phi_\Gamma}{\phi} h^2 n_y \right] \mathrm{d}\Gamma \\
&= \phi \tfrac{\mathrm{d}y}{\cos\alpha} \left[\tfrac{\phi}{\phi_1} (q\cos\alpha + r\sin\alpha) \tfrac{r}{h} + \tfrac{\phi_1}{\phi} \sin\alpha \tfrac{g}{2} h^2 \right]_{x+\frac{\mathrm{d}x}{2}, y} \\
&\quad - \phi \tfrac{\mathrm{d}y}{\cos\alpha} \left[\tfrac{\phi}{\phi_1} (q\cos\alpha + r\sin\alpha) \tfrac{r}{h} + \tfrac{\phi_1}{\phi} \sin\alpha \tfrac{g}{2} h^2 \right]_{x-\frac{\mathrm{d}x}{2}, y} \\
&\quad + \phi \mathrm{d}x \left[\tfrac{\phi}{\phi_2} \tfrac{r^2}{h} + \tfrac{\phi_2}{\phi} \tfrac{g}{2} h^2 \right]_{x-\frac{\mathrm{d}y}{2}\tan\alpha, y+\frac{\mathrm{d}y}{2}} - \phi \mathrm{d}x \left[\tfrac{\phi}{\phi_2} \tfrac{r^2}{h} + \tfrac{\phi_2}{\phi} \tfrac{g}{2} h^2 \right]_{x+\frac{\mathrm{d}y}{2}\tan\alpha, y-\frac{\mathrm{d}y}{2}} \\
&= \phi \mathrm{d}x\mathrm{d}y \partial_x \left[\tfrac{\phi}{\phi_1} \tfrac{qr}{h} + \left(\tfrac{\phi}{\phi_1} - \tfrac{\phi}{\phi_2} \right) \tan\alpha \tfrac{r^2}{h} + \tfrac{\phi_1 - \phi_2 \tan\alpha}{\phi} \tfrac{g}{2} h^2 \right] + \phi \mathrm{d}x\mathrm{d}y \partial_y \left(\tfrac{\phi}{\phi_2} \tfrac{r^2}{h} + \tfrac{\phi_2}{\phi} \tfrac{g}{2} h^2 \right)
\end{aligned} \tag{61}$$

hence the $y-$momentum equation

$$\partial_t r + \partial_x \left[\frac{\phi}{\phi_1} \frac{qr}{h} + \left(\frac{\phi}{\phi_1} - \frac{\phi}{\phi_2} \right) \tan\alpha \frac{r^2}{h} + \frac{(\phi_1 - \phi_2)\tan\alpha}{\phi} \frac{g}{2} h^2 \right] + \partial_y \left(\frac{\phi}{\phi_2} \frac{r^2}{h} + \frac{\phi_2}{\phi} \frac{g}{2} h^2 \right) = 0 \tag{62}$$

A.2.3 Jacobian matrices

The Jacobian matrices $\mathbf{A}_x$ and $\mathbf{A}_y$ are obtained by differentiating the flux tensor obtained from equations (55, 60, 62) with respect to the conserved variable:

$$\mathbf{A}_x = \begin{bmatrix} 0 & 1 & 0 \\ \epsilon_1 c^2 - \frac{u^2}{\epsilon_1} - \epsilon_6 uv & \frac{2u}{\epsilon_1} + \epsilon_6 v & \epsilon_6 u \\ \epsilon_3 c^2 - \frac{uv}{\epsilon_1} - \epsilon_6 v^2 & \frac{v}{\epsilon_1} & \frac{u}{\epsilon_1} + 2\epsilon_6 v \end{bmatrix} \tag{63a}$$

$$\mathbf{A}_y = \begin{bmatrix} 0 & 0 & 1 \\ -\frac{uv}{\epsilon_2} & \frac{v}{\epsilon_2} & \frac{u}{\epsilon_2} \\ \epsilon_2 c^2 - \frac{v^2}{\epsilon_2} & 0 & \frac{2v}{\epsilon_2} \end{bmatrix} \tag{63b}$$

A.3 Numerical determination of the eigenvalues of $\mathbf{A}_\theta$

Noticing that the upper left element of the matrix $\mathbf{A}_\theta$ is zero, the eigenvalues λ of the matrix are solutions of the characteristic polynomial

$$f(\lambda) = \lambda^3 + A\lambda^2 + B\lambda + C = 0 \tag{64a}$$

$$A = -(a_{22} + a_{33}) \tag{64b}$$

$$B = a_{22}a_{33} - a_{23}a_{32} - a_{21}a_{12} - a_{13}a_{31} \tag{64c}$$

$$C = (a_{12}a_{33} - a_{32}a_{13})\, a_{21} + (a_{22}a_{13} - a_{12}a_{23})\, a_{31} \tag{64d}$$

The roots of equation (64a) are found numerically using Newton's method. The derivative of the characteristic polynomial cancels for

$$\lambda_e = \frac{1}{3}\left(-A \pm \left(A^2 - 3B\right)^{\frac{1}{2}}\right) \tag{65}$$

If the characteristic polynomial has three roots, the first one is necessarily smaller than the smaller of the two $\lambda_e$values, the second is between these two λ_e and the third is necessarily larger than the large of the two λ_e. A Newton procedure is used, with the following three initial starting points:

$$\lambda_{p,\text{init}} = \left(-A + 2\,(p-2)\left(A^2 - 3B\right)^{\frac{1}{2}}\right), \quad p = 1, 2, 3 \tag{66}$$

The factor 2 in front of $(p-2)$ ensures that the starting points are significantly different from λ_e and a non-zero derivative is obtained for the initial values of λ_1 and λ_3. The iterations are stopped when the absolute of $f(\lambda)$ is smaller than 10^{-12}.

References

[1] Benkhaldoun, F., Elmahi, I., Moumna, A., Seaid, M. 2016. A non-homogeneous Riemann solver for shallow water equations in porous media. Applicable Analysis 95, 2181-2202, DOI:

10.1080/00036811.2015.1067304.

[2] Cea, L., Vazquez-Cendon, M.E. 2010. Unstructured finite volume discretization of two-dimensional depth-averaged shallow water equations with porosity. Int J Numer Methods Fluids 63, 903–30.

[3] Cunge, J.A. 1969. On the subject of a flood propagation computation method (Muskingum method). Journal of Hydraulic Research 7(2): 205-230.

[4] Daubert, A., Graffe, O. 1967. Quelques aspects des écoulements presque horizontaux a deux dimensions en plan et non permanents. Application aux estuaires. La Houille Blanche 22(8), 847–860, 1967 (in French).

[5] Defina, A. 2000. Two-dimensional shallow flow equations for partially dry areas. Water Resour Res 36, 3251–64.

[6] Finaud-Guyot, P. Delenne, C., Lhomme, J., Guinot, V., Llovel, C. 2010. An approximate-state Riemann solver for the two-dimensional shallow water equations with porosity. International Journal for Numerical Methods in Fluids 62, 1299–1331.

[7] Guinot, V. 2003. Riemann solvers and boundary conditions for two-dimensional shallow water simulations. International Journal for Numerical Methods in Fluids 41, 1191-1219.

[8] Guinot, V. 2010. Wave propagation in Fluids. Models and numerical techniques. Wiley-ISTE.

[9] Guinot, V. 2012. Multiple porosity shallow water models for macroscopic modelling of urban floods. Advances in Water Resources 37, 40-72.

[10] Guinot, V., Delenne, C. 2014. Macroscopic modelling of urban floods. La Houille Blanche 6, 19-25.

[11] Guinot, V., Soares-Frazão, S. 2006. Flux and source term discretization in shallow water models with porosity on unstructured grids. Int J Numer Methods Fluids 50, 309–45.

[12] Guinot, V., Sanders, B.F., Schubert, J. 2017. Dual integral porosity shallow water model for urban flood modelling. Advances in Water Resources 2017, 103, 16-31

[13] Hervouët, J.M., Samie, R., Moreau, B. 2000. Modelling urban areas in dam-break floodwave numerical simulations. In: Proceedings of the international seminar and workshop on rescue actions based on dambreak flow analysis, Seinâjoki, Finland, 1–6 October 2000.

[14] Kim, B., Sanders, B.F., Famiglietti, J.S., Guinot, V. 2015. Urban flood modeling with porous shallow-water equations: A case study of model errors in the presence of anisotropic porosity. Journal of Hydrology 523, 680-692.

[15] Lhomme, J. 2006. Modélisation des inondations en milieu urbain. Approches unidimensionnelle, bidimensionnelle et macroscopique. PhD thesis. University Montpellier 2 (in French).

[16] Özgen, I., Liang, D., Hinkelmann, R. 2016. Shallow water equations with depth-dependent anisotropic porosity for subgrid-scale topography. Applied Mathematical Modelling 40, 7447-7473.

[17] Özgen, I., Zhao J., Liang D., Hinkelmann R. 2016. Urban flood modeling using shallow water equations with depth-dependent anisotropic porosity. Journal of Hydrology, 541, 1165-1184.

[18] Sanders, B.F., Schubert, J.E., Gallegos, H.A. 2008. Integral formulation of shallow water equations with anisotropic porosity for urban flood modelling. J Hydrol. 362, 19–38.

[19] Schubert, J.E., Sanders, B.F. 2012. Building treatments for urban flood inundation models and implications for predictive skill and modeling efficiency. Advances in Water Resources 41, 49-64.

[20] Soares-Frazao, S., Lhomme, J., Guinot, V., Zech, Y. 2008. Two–dimensional shallow water models with porosity for urban flood modelling. Journal of Hydraulic Research 46(1), 45-64.

[21] Viero, D. P., Mohammad Valipour, M. 2017. Modeling anisotropy in free-surface overland and shallow inundation flows. Advances in Water Resources, 104, 1–14.